Geophys. J. Int. (1990) **103,** 589–598

The 1960 Chile earthquake: inversion for slip distribution from surface deformation

Sergio E. Barrientos[1] and Steven N. Ward[2]

[1]Dpto. de Geología y Geofísica, Universidad de Chile, Santiago, Chile
[2]C. F. Richter Laboratory/Institute of Tectonics, University of California at Santa Cruz, CA 95064, USA

Accepted 1990 June 15. Received 1990 May 21; in original form 1989 August 14

SUMMARY

A total of 166 observations of sea-level change, 130 measurements of elevation difference, and 16 determinations of horizontal strain provide an excellent view of the (quasi-)static source process of the great 1960 Chilean earthquake. These surface deformation data were employed in classical uniform slip fault models as well as more recently developed models that allow spatial variability of slip. The best uniform slip planar (USP) model is 850 km long, 130 km wide, and dips 20°. Seventeen metres of fault displacement contributed to a USP moment of 9.4×10^{22} N m. The variable slip planar (VSP) model concentrates slip on a 900 km long, 150 km wide band parallel to the coast. Several peaks of slip with dimensions of 50–100 km appear in this band and are thought to represent major subduction zone asperities. Important fractures of the oceanic lithosphere bound the 1960 rupture and are offered as a potential source of fault segmentation within the Chilean subduction zone. The VSP moment for 1960 earthquake totals 9.5×10^{22} N m, about one fifth of the value estimated for the foreshock–mainshock sequence from seismic methods. Except for areas out to sea, geodetic resolution on the fault is fairly uniform. Thus, it is unlikely that slip missed by the network could increase the VSP moment much beyond 1.8×10^{23} N m. Several patches of moment, isolated from the main body at 80–110 km depth, are found down dip in the VSP model and are presumably indicative of aseismic slip. One patch at the northern end of the rupture is probably associated with the initiation phase of the mainshock, although the time sequence of the relationship is unknown. Tide gauge records suggest that another patch between 40° and 43° S, responsible for the observed strain and uplifts inland at those latitudes, is not of coseismic origin, but derives from in-place, post-seismic creep over several years. Apparently, great 1960-type events are not typical members of the ≈128 yr earthquake cycle in south-central Chile. The Nazca–South America boundary here is characterized by a variable rupture mode in which major asperities are completely broken by great earthquakes only once in four or five earthquake cycles. The more frequent large earthquakes, that geographically overlap the great events, fill in between the locked zones.

Key words: Chile: 1960 earthquake, earthquake geodesy, fault slip patterns.

1 INTRODUCTION

The great Chilean earthquake of 1960 May 22, with a surface wave magnitude of 8.5 and a moment magnitude of 9.5, was the largest event recorded this century (Kanamori 1977). The quake and subsequent tsunami affected a disaster region inhabited by two and a half million people, caused over two thousand fatalities, and damaged property valued between 500 and 700 million dollars (Sievers, Villegas & Barros 1963; Housner 1963). Nearly all of the important cities in south-central Chile from Concepción to Puerto Montt (Fig. 1) suffered severe damage from shaking which exceeded intensity VIII (Modified Mercalli Scale). Soil liquefaction and surface failure were widespread. At one point a large landslide blocked the outflow of Riñihue Lake, raised the water level 26.5 m, and endangered the city of

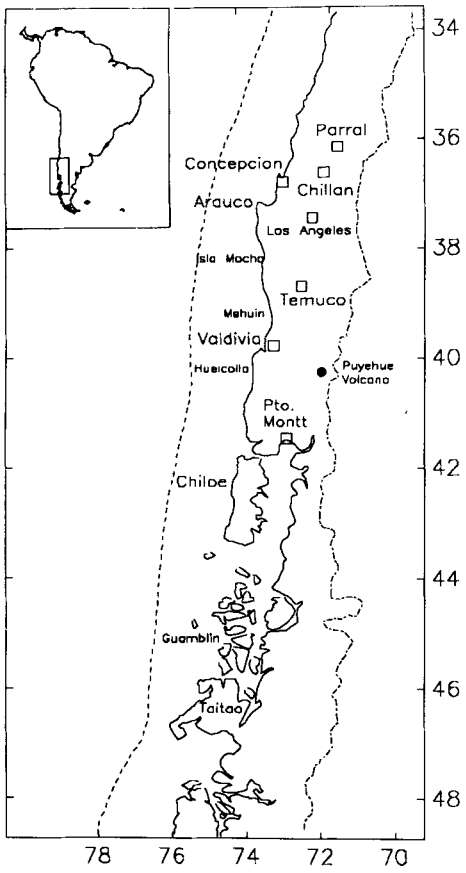

Figure 1. Site of the great 1960 Chile earthquake. Surface deformation extended from the city of Concepción in the north to the Taitao Peninsula in the south. The dashed line to the west is the axis of the Chile Trench.

Valdivia, 65 km to the west (Duke & Leeds 1963; Davis & Karzulovíc 1963; Wieschet 1963; Wright & Mella 1963). Eruptions of Puyehue volcano began two days after the mainshock and steadily increased in violence for 7 days. The earthquake-induced tsunami spread over the Pacific Ocean causing hundreds of deaths as far away as Japan. Locally, the wave reached heights of 10 m, wreaked havoc on shore facilities and scrubbed several villages from the Earth. At the Bay of Corral, just west of Valdivia, a tug and three freight ships were dragged repeatedly several kilometres in and out of the harbor. Two of the freighters eventually lost their bottoms and were sunk, one at a point 5 km up Rio Valdivia from its original mooring. The tug was drawn into a turbulent trough of water some 8 m deep during the withdrawal of one of the waves, did a double somersault, and disappeared completely. Remarkable changes in land levels associated with the great 1960 shock were observed over an area 200 km wide and 1000 km long stretching northward from the Taitao Peninsula. In Valdivia Province, over 15 000 hectares of settled and agricultural land were submerged. This paper investigates details of the 1960 faulting as revealed by these surface movements. For this, we employ classical uniform slip models of earthquake faults as well as more recently developed models that allow spatial variability of slip.

2 SEISMIC HISTORY OF THE 1960 SEQUENCE

The 1960 mainshock was a complicated rupture that lasted for several minutes. The event was third in a sequence of major earthquakes within a 33 hr period. The sequence initiated with a 7.5 ISC magnitude earthquake at 10 02 hr on May 21 followed on May 22 by a 7.8 shock at 18 55 hr. The mainshock occurred 15 min later and consisted largely of two 8.3 subevents at 19 10 and 19 11 hr (Duda 1963). According to Lomnitz & Hax (1966) and Lomnitz (1970), cited in Plafker & Savage (1970), the two foreshocks (A and B in Fig. 2) located progressively closer to the mainshock (C and D in Fig. 2). Cifuentes (1989) relocated several pre- and aftershocks of the sequence and proposed that events A–D actually happened on a line trending N30°W, some 100 to 200 km northeast from Duda's locations (see Fig. 2).

Based on free oscillation spectra and analyses of long-period mantle Rayleigh and *G*-waves, Press *et al.* (1961) concluded that the 1960 rupture traversed 1000 km of fault at the velocity of crustal shear waves. Using *R2*- and *G2*-waves (230 s period) from a Pasadena long-period strain seismogram, Kanamori & Cipar (1974) estimated the

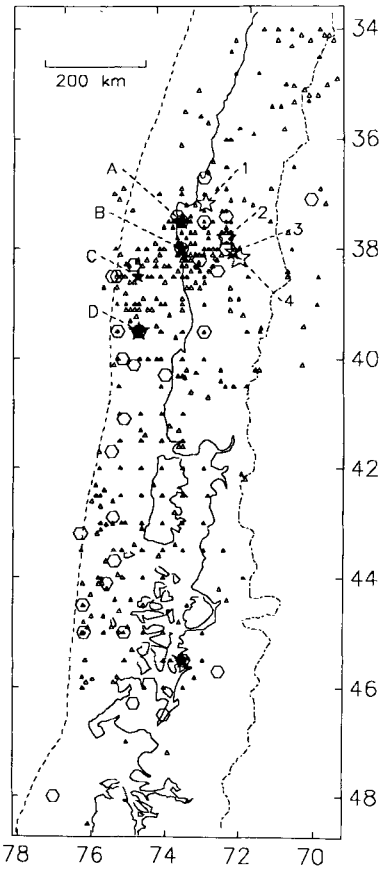

Figure 2. ISC seismicity for 1960–1968. The hexagons and triangles correspond to aftershocks with magnitudes greater and less than 6.0 respectively. Most of the aftershock activity lies in the region offshore east of the trench. The stars marked A, B, C, and D are epicentres of the major events in the 1960 sequence (Duda 1963). Stars numbered 1, 2, 3, and 4 are the positions of the same events as determined by Cifuentes (1989).

seismic moment of the 1960 mainshock (C plus D) to be 2.7×10^{23} N m with an average dislocation of 24 m. They suggested that the precursory event (B) also had about the same moment and occurred down dip of the mainshock. Kanamori (1977) later revised the mainshock moment down to 2.0×10^{23} N m. Cifuentes & Silver (1989) concluded that the B, and C plus D sequence had moments of 1.9 and 3.2×10^{23} N m.

The ISC reported more than 500 aftershocks in the eight years following the main event. Most of the activity centred at the northern end of the rupture near Concepción (Herron 1981). To the south, most of the seismicity is restricted within a 300 km wide strip landward of the trench and north of Taitao Peninsula. Most of the aftershocks with magnitudes greater than 6.0 (hexagons in Fig. 2) locate offshore east of the trench. Barazangi & Isacks (1976) studied the pattern of seismicity along the South American western margin and noted that between 38°S and 45°S, seismicity is largely confined to depths less than 70 km.

3 SEA LEVEL, LEVELLING, AND TRIANGULATION DATA

George Plafker of the US Geological Survey visited the site of the mainshock eight years after the event and measured 'coseismic' (1968–1960) sea-level changes at more than 150 localities. He based his observations on: the pre- and post-seismic lower growth limit of terrestrial vegetation; the upper growth limits of pre- and post-earthquake mussels; and the position of post-earthquake high tide lines relative to pre-earthquake levels reported by local residents. Care was taken to restrict observations to bedrock sites to minimize the effects of subsidence due to surficial compaction and slumping of unconsolidated materials. The root mean square (rms) displacement and error for the 166 measurements are 1.24 and 0.31 m respectively. Extreme coseismic sea level changes ranged from 5.7 m of uplift in Guamblin Island to 2.7 m of subsidence in the city of Valdivia.

Plafker & Savage (1970) analysed the static deformation data and presented teleseismic surface wave evidence to support their preferred uniform slip dislocation model that involves between 20 and 40 m of dip slip on a fault 1000 km long and at least 60 km wide. The total moment for their model ranges from 0.6 to 1.2×10^{23} N m (assuming $\mu = 5 \times 10^{10}$ Pa). Plafker (1972) reanalysed the static deformation and deduced a causative fault 120 km wide by 1000 km long, dipping 20°E with 20 m of slip.

To model the slip pattern of the 1960 earthquakes, this paper considers Plafker & Savage's sea-level measurements together with 130 additional points from a first-order levelling line and 16 strain measurements from eight triangulation networks in Chile's central valley. Pre-earthquake levelling along a line running 150 km northeast from the coastal city of Concepción to Parral, and 600 km south to Puerto Montt (Fig. 3) was done in 1957–1959. The post-earthquake survey was carried out in 1963–1964. A conservative estimate of the uncertainty in elevation difference between the ends of the line is 0.18 m. Rms displacement and error for the levelling data are 1.02 and 0.13 m. Extreme coseismic elevation changes were +0.1 m and −2.5 m. The eight, first-order triangulation surveys,

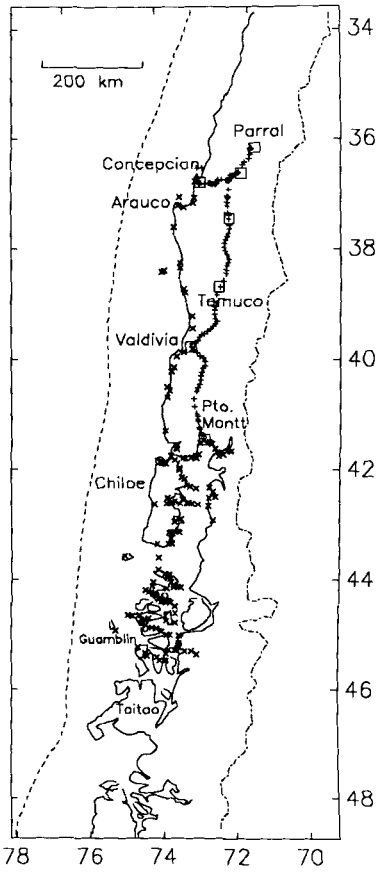

Figure 3. Locations of measured vertical elevation change. Vertical crosses stretching from Concepción to Puerto Montt are benchmarks levelled in 1957–1959 and 1963–1964. Diagonal crosses are sites where Plafker estimated sea-level changes in 1968.

supplemented by second-order stations, were carried out by the Instituto Geográfico Militar in 1950–1952. A post-seismic survey (1966–1968) of the same stations enabled Plafker & Savage (1970) to compute surface shear strains (Fig. 8). Rms strain and error are 32.7×10^{-6} and 10.4×10^{-6}.

Because individual sea-level, levelling and strain data can have greatly different uncertainties, weighted least-square norms are employed to judge model quality. The weights for the individual measurements are inversely proportional to their estimated error σ_i. For the sea-level data, σ_i are the uncertainties quoted by Plafker & Savage (1970). They rated their observations as good (±0.2 m), fair (±0.4 m), and poor (±0.6 m). Uncertainties for the levelling data were fixed at $\sigma_i = 0.13$ m. Errors in strains were taken to be one half the values quoted by Plafker & Savage (1970). (The increased weight produces a slightly more equitable distribution of misfit in the models below.) Chi-square (χ^2) variance for the sea-level, levelling and strain data are 4059, 8022 and 2206 respectively. Models consistent with the observational error within 1σ should have χ^2s equal to 166, 130 and 16; the number of data in each class.

4 MATHEMATICAL APPROACH

The forward problem in analysing surface deformation data resulting from slip on spatially finite faults considers

displacement component $u_i(\mathbf{r})$ at a point $\mathbf{r}$ on the Earth's surface to be

$$u_i(\mathbf{r}) = \int_A K(\mathbf{r}, \mathbf{r}^0)\hat{m}(\mathbf{r}^0)\, d\mathbf{r}^0 \quad (1)$$

where $\int d\mathbf{r}^0$ covers all points on the fault surface A, and $\hat{m}(\mathbf{r}^0)$ is moment density, a function of position. The sensitivity kernel $K(\mathbf{r}, \mathbf{r}^0)$ is a function of specified fault parameters (strike, dip and rake) and the relative positions of $\mathbf{r}$ and $\mathbf{r}^0$. Ward & Barrientos (1986) give $K(\mathbf{r}, \mathbf{r}^0)$ for u_z in a uniform, non-gravitating elastic half-space. The Appendix of this paper gives the kernel for u_r and u_θ under similar assumptions. In practice, $\hat{m}(\mathbf{r}^0)$ is discretized into N elementary sources and the data are composed of M observations. Equation (1) reduces to

$$u(\mathbf{r}_i) = \sum_{j=1}^{N} K(\mathbf{r}_i, \mathbf{r}_j^0)m(\mathbf{r}_j^0) \quad (2)$$

or

$$u(\mathbf{r}_i) = \sum_{j=1}^{N} \hat{K}(\mathbf{r}_i, \mathbf{r}_j^0)s(\mathbf{r}_j^0) \quad (3)$$

if each source is associated with fault area δA_j and an unknown slip s_j.

Uniform slip planar (USP) models

The first step in our approach finds the best fitting uniform slip, plane rectangular fault (USP). The best USP fault provides both a standard with which to compare more complex models and the orientation of the surface over which variable slip will later be permitted. The complete formulation of the USP model involves 10 unknowns: strike, dip and rake angles; fault slip; length along-strike and width along-dip; the x, y and z position of an upper fault corner; and a static baseline correction for the levelling data u_0.

All of the USP parameters have a non-linear effect on the data, except for slip and u_0, and it is unlikely that all 10 parameters can be recovered in an unrestricted inversion. Our approach is to constrain some parameters thought to be more certain and to estimate the remaining ones in a straightforward search procedure. We chose to fix the strike and rake angle and search for the position of the fault, length, width and dip. Because the trace of the 1960 event cannot be recognized on the surface, the strike of the fault was assumed to coincide with the local trend (N7°E) of the Peru–Chile trench. The rake angle of the event was fixed at 105°, the long-term direction of relative motion between the Nazca and South America plates predicted by the RM2 model of Minster & Jordan (1978). The depth of the upper southern corner was fixed at 4 km.

The best USP fault (Fig. 4) dips 20°E and extends 850 km south from the Arauco Peninsula. The best southern endpoint is near the Taito Peninsula. This point is not well constrained due to the lack of information south of 45.3°S; however, reports of uplift in the northern edge of the Peninsula (CERESIS 1986) suggest that faulting reached at least that far south. Seventeen metres of displacement on the 130 km wide fault contributed to a USP moment of 9.4×10^{22} N m ($\lambda = \mu = 5 \times 10^{10}$ Pa). Our best USP fault does not differ notably from Plafker's (1972) model. Fig. 5 shows the USP fit to the vertical deformation data. The top four panels are projections of the observed and predicted sea-level changes on a west to east plane for the latitude ranges: 41.5°–42.5°S, 42.5°–43.5°S, 43.5°–44.5°S, and 44.5°–45.5°S. The bottom two panels are projections of the observed and predicted sea-level and levelling data on a north–south plane from Concepción to Puerto Montt. χ^2 fits for the USP model are 1245, 1734 and 391; up to 24 times larger than expected given the uncertainties in the data. We suppose that the excess USP residuals result from the simplification of uniform slip.

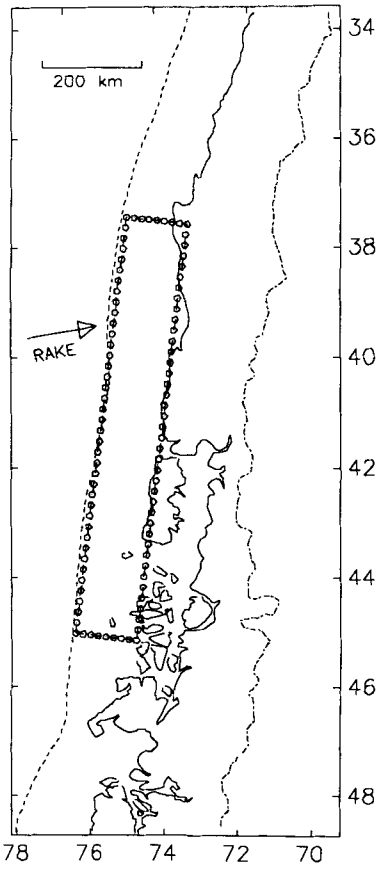

Figure 4. Map view of the outline of the best USP fault model. The fault is 850 km long, 130 km wide, dips 20° and has 17 m of displacement. Most of the slip is located offshore toward the trench.

Variable slip planar (VSP) models

Variable slip analyses of surface deformation were first applied to the 1983, Borah Peak, Idaho event by Ward & Barrientos (1986). The method was later applied to the 1985 Central Chile (Barrientos 1988) and the 1915 Avezzano, Italy, (Ward & Valensise 1989) earthquakes. In matrix form, the linear problem describing the moment distribution (2) is

$$\underset{(M\times 1)}{\mathbf{u}} = \underset{(M\times N)}{\mathbf{K}}\ \underset{(N\times 1)}{\mathbf{m}}. \quad (4)$$

In VSP models, the number of elemental sources distributed on the fault generally far outnumber the available data. Provided that (4) is consistent ($\mathbf{K}\mathbf{K}^{-1}\mathbf{u} = \mathbf{u}$), a complete set

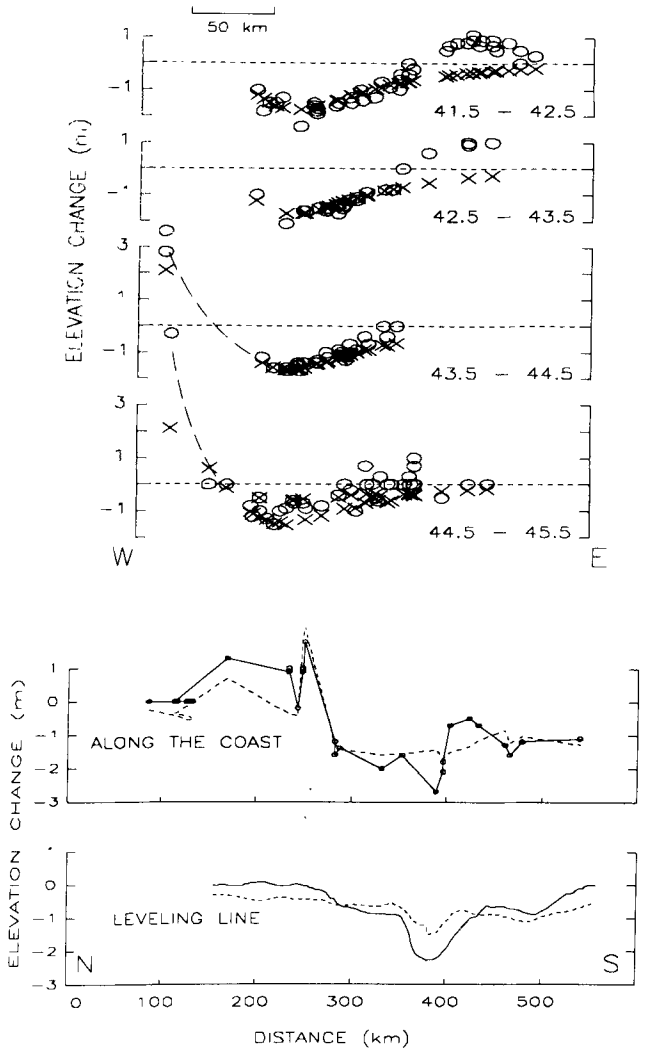

Figure 5. Fit of the best USP model to the vertical deformation data. The top four panels show observed (circles) and predicted (crosses) sea-level changes on selected profiles perpendicular to the trench. The bottom two panels show sea-level and levelling data parallel to strike along the coast and in the central valley. Dashed lines are the predictions. Note the systematic misfit of the inland observations toward the right of the two upper panels. Misfits in the bottom two panels point to slip variations along strike.

of exact solutions can be formed as

$$\mathbf{m} = \mathbf{K}^{-1}\mathbf{u} + (\mathbf{I} - \mathbf{K}^{-1}\mathbf{K})\mathbf{m}_{\mathbf{m}}, \tag{5}$$

where $\mathbf{K}^{-1}$ is any matrix satisfying $\mathbf{K} = \mathbf{K}\mathbf{K}^{-1}\mathbf{K}$ and $\mathbf{m}_{\mathbf{m}}$ is any $(N \times 1)$ vector. The second term in (5) represents the class of slip distributions which produce no signal at any site in the net. For arbitrary $\mathbf{K}^{-1}$ and $\mathbf{m}_{\mathbf{m}}$, exact solutions (5) will be extremely ragged, fraught with large and narrow peaks of positive and negative slip.

The VSP method employs an iterative gradient technique and a positivity constraint to subdue objectionable aspects of an arbitrary solution (5). The nth VSP model is

$$\begin{aligned}\mathbf{m}^n_{\mathrm{Gpos}} &= [\mathbf{m}^{n-1}_{\mathrm{Gpos}} + \Delta m \mathbf{K}^{\mathrm{T}}(\mathbf{u} - \mathbf{K}\mathbf{m}^{n-1}_{\mathrm{Gpos}})]_{\mathrm{pos}} \\ &= [\mathbf{m}^{n-1}_{\mathrm{Gpos}} - \frac{\Delta m}{2}\nabla E^2(\mathbf{m}^{n-1}_{\mathrm{Gpos}})]_{\mathrm{pos}},\end{aligned} \tag{6}$$

where $[]_{\mathrm{pos}}$ signifies the positive part. The increment to the solution, the second term of the right side, is proportional to the gradient of squared error in $\mathbf{m}^{n-1}_{\mathrm{Gpos}}$ (hence the name of the method). In this application, the positivity constraint is applied at each iteration starting with $\mathbf{m}^0_{\mathrm{Gpos}} = \mathbf{0}$. If Δm is sufficiently small, $E^2(\mathbf{m}^n_{\mathrm{Gpos}}) < E^2(\mathbf{m}^{n-1}_{\mathrm{Gpos}})$ and the process continues until improvements effectively stop or until the misfit equals the error in the data. Inversion (6) is performed with sources $\mathbf{m}$, distributed on the USP fault over an area much larger than the expected region of slip.

The final VSP model (Fig. 6) of the 1960 earthquake concentrates most of the moment release offshore in a 900 km long, 150 km wide band parallel to the coast. Fault area and average slip within the 1 m contour are 2.2×10^5 km^2 and 8.0 m; about twice as large and 50 per cent less than the USP results respectively. Mean static stress drop ($\Delta\tau = \mu\Delta\bar{u}/\sqrt{A}$) for the event is 0.85 MPa (8.5 bar). A punctuated ridge of high slip, peaking at 41 m occurs at a depth of 34 km just at the shoreline. Total moment for the event is 9.5×10^{22} N m, consistent with previous geodetic estimates but less than one fifth of the total seismic moment of the 1960 sequence (events B, C and D) estimated by Kanamori & Cipar (1974) and Cifuentes & Silver (1989). Moment release in the main slip body terminates sharply at 51 km depth, the probable lower limit of locking in the interplate thrust zone (Tichelaar & Ruff 1989).

The distribution of peaks and patches of high slip (and high static stress drop) are of particular interest. The patches range in size from 50 to 200 km and possess slips two or three times the average. Peaks falling at shallow depths in the main body of moment release are thought to be rupture-controlling asperities. Local static stress drops in these asperities reach 68.5 MPa (685 bar). Other down dip patches, disconnected from the main body at depths of 80–110 km, are presumably indicative of aseismic slip. Cifuentes' epicentres hint that the nucleation phase of the mainshock or its immediate precursors are associated with one of these patches toward the northern end of the rupture (Fig. 6, right).

The VSP uplift predictions are displayed in Fig. 7. The systematic misfits produced by the USP model now disappear. Observed principal strains (Fig. 8), except for network E, are also reproduced. χ^2 misfit of the VSP model for the three data classes are 172, 127 and 12; much improved from the USP result and consistent with the data error at 1σ.

Model resolution

Stability and resolution of VSP slip patterns were extensively investigated by Ward & Valensise (1989). We consider one of their criteria, combined geodetic resolution

$$L^{\min}(\mathbf{r}^0) = \sqrt{\frac{(1/s^{\min})}{\mu R(\mathbf{r}^0)}}, \tag{7}$$

where

$$R(\mathbf{r}^0) = \sqrt{N^{-1}\sum_{i=1}^{N} K^2(\mathbf{r}_i, \mathbf{r}^0)/\sigma_i^2} \tag{8}$$

is the weighted rms sensitivity kernel. $L^{\min}(\mathbf{r}^0)$ is an estimate

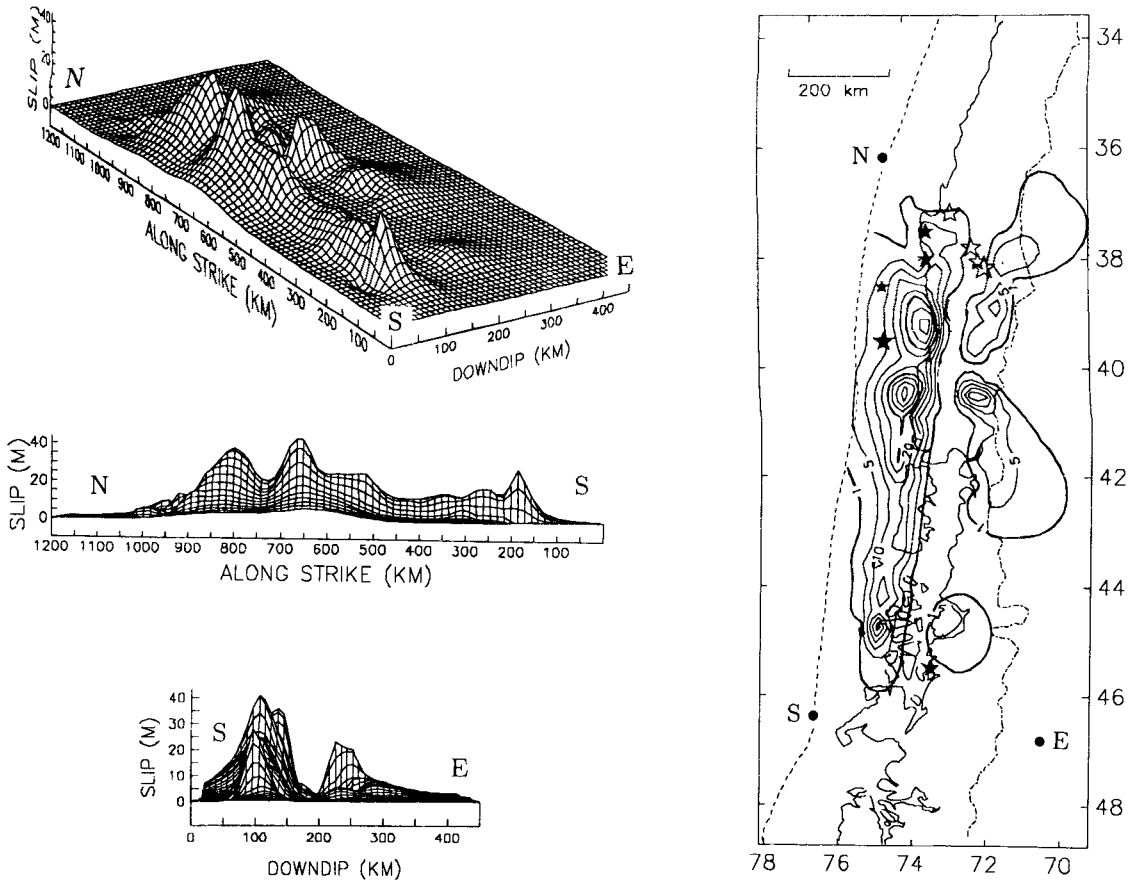

Figure 6. Four views of the VSP slip distribution of the 1960 event. The rupture, modelled with 600 sources, is approximately 900 km long, 150 km wide, with maximum slip exceeding 40 m. Most of the slip is centred 50–150 km down dip from the trench. Note the three patches of slip isolated 100 km down dip from the main zone of moment release. The most northerly of these is likely to be associated with the foreshocks and nucleation phase of the mainshock. Tide gauge data suggests that the central down dip patch results from slow, post-seismic creep.

of the scale length of resolvable features with characteristic slip $s^{\min}$ at point $\mathbf{r}^0$ on the fault from a survey of a specified precision. As σ_i grows in less precise surveys, the size of resolvable features must increase for a characteristic slip, or, characteristic slip must increase on resolvable features of fixed size. Slip at points $\mathbf{r}_i^0$ and $\mathbf{r}_j^0$ which share the same value of $L^{\min}$ should be equally well resolved.

Figure 9 contours $L^{\min}(\mathbf{r}^0)$ in km for $s^{\min} = 5$ m. Resolution of the network is surprisingly uniform over a 900 by 250 km rectangle starting about 50 km down dip. None of the observed patches of slip is more compact than the resolution scale appropriate for their individual amplitudes and locations. In VSP models, details of slip patterns which are generated solely by the geometry of the network should be mirrored in $L^{\min}$. Because few of the significant features in the VSP model correspond to features in the resolution, we have confidence in the picture.

5 MODEL IMPLICATIONS AND DISCUSSION

Role of fracture zones in fault segmentation

At least nine major fracture zones are present on the subducting Nazca plate (Fig. 10). Some of these fractures bound seafloor of significantly different age. The Valdivia and Mocha fractures, for example, delimit the Mocha Island Block (Herron 1981). Seafloor just south of the Block was formed at the East Pacific Rise some 20 Myr ago. Just north of the Mocha block, the seafloor is nearly twice as old, having formed at the now extinct Pacific–Farallon spreading centre. Inland extensions of both fractures correlate with local geomorphology and coincide with two right-lateral steppings of the border between Argentina and Chile which is formed by line segments joining the highest peaks of the Andes. Further to the south, the closely spaced Guamblin and Darwin fracture zones just north of Taitao Peninsula also produce similar indentations.

If certain fractures define regions of different age and mechanical properties, they might also delimit regions of different slip behaviour on the interplate thrust zone (Herron 1981). Overlays of the VSP slip pattern and the landward extension of these fracture zones (Fig. 10) show that the 1960 rupture was sharply bounded to the north by the Mocha, and to the south by the Guamblin and Darwin fractures. Nucleation of the 1960 events, as evidenced by their epicentral locations (stars, Fig. 10), also coincides with the northern terminus of the rupture near the Mocha fracture. We propose that certain seafloor fractures can act as geometrical barriers to rupture and concentrators of

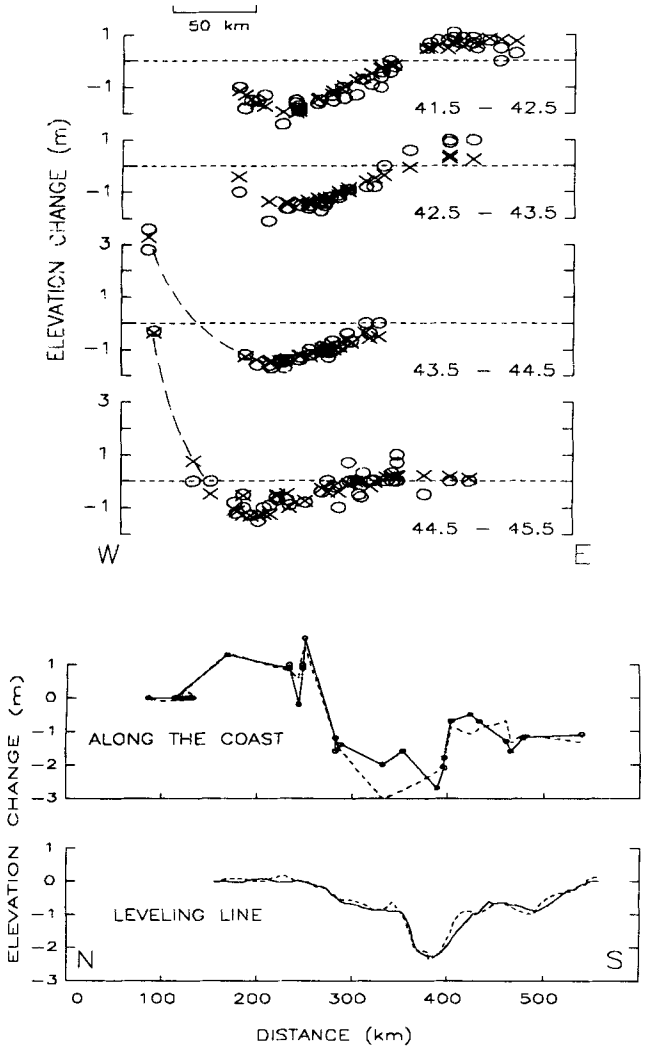

Figure 7. Fit of the best VSP model to the vertical deformation data. In contrast to the USP result in Fig. 5, little systematic misfit is seen in the top or bottom two panels. The largest misfit of the sea-level data along the coast occurs close to the point of maximum subsidence, near Valdivia, and may reflect a non-tectonic process.

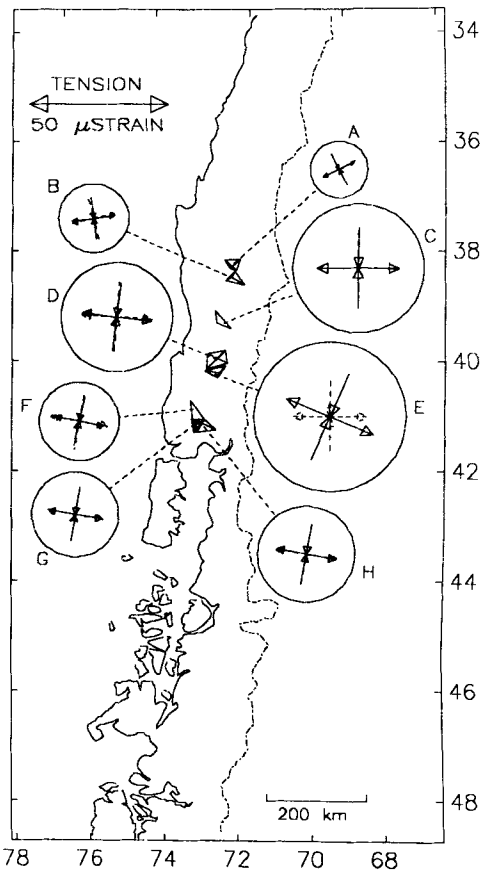

Figure 8. Comparison of observed surface strains (solid arrows) from Plafker & Savage (1970) with those predicted by the VSP model (dashed arrows). Except for network 'E', directions and magnitudes of the strains at all eight sites are well reproduced.

stress, much like restraining bends in strike slip environments. If the correlation between fracture zones and segmentation of earthquake behaviour in subduction zones can be further validated, it would be a major aid in understanding earthquake dynamics, in categorizing characteristic events, and in localizing seismic and geodetic experiments.

Convergence rate and recurrence intervals

History documents that large earthquakes strike south-central Chile roughly every century. For example, near Concepción, at the northern end of the 1960 rupture, previously large shocks occurred in 1570, 1657, 1751, and 1835. Near Valdivia–Chiloé, in the central segment of the 1960 rupture, events with $M > 8$ were noted in 1575, 1737, and 1837 (Lomnitz 1970). Nishenko (1985) estimated rupture lengths between 700 and 1000 km and an average repeat time of 128 ± 31 yr for these events. Likely rates of convergence of the Nazca and South America plates over geologic time range from 11 cm yr^{-1} (RM2, Minster & Jordan 1978) to 8.4 cm yr^{-1} (NUVEL-1, DeMets *et al.* 1990). Conservatively, a totally coupled boundary would accumulate 11 m of slip after 128 yr. Eleven metres is close to the average slip found above the 1 m contour for the 1960 earthquake, although certain patches had slips over 40 m. To be consistent with plate convergence rates, these patches could break completely in only every fourth or fifth event. Apparently, great 1960-type earthquakes are atypical members of 128 yr cycle. Stein *et al.* (1986) came to a similar conclusion by comparing plate motion models with observed slip rates. The dichotomy of repeating large and occasional great earthquakes overlapping in space can be explained in terms of a variable rupture mode (Kanamori & McNally 1982; Cifuentes 1989) and visualized in the VSP models. The Chilean subduction process exhibits two classes of behaviour; great 1960-type earthquakes with recurrence times of ≈500 yr which rupture large asperities unbroken for several past cycles, and more common large earthquakes with repeat times of ≈150 yr whose smaller ruptures fill in areas between major asperities.

Post-seismic movements?

One curious feature of Fig. 9 is the isolated patches of slip 150–200 km down dip from the main moment release. These

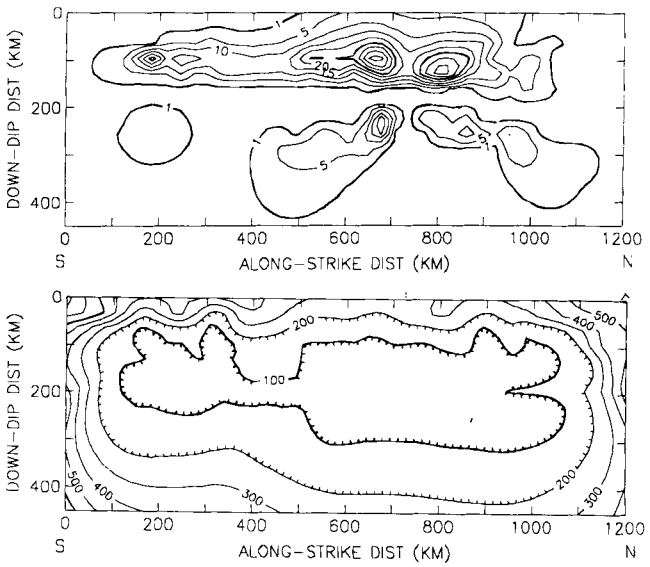

Figure 9. Top: contour map of fault slip for the VSP model. Contours are 1, 5, 10, . . . , 35 and 40 m. Bottom: combined geodetic resolution $L^{\min}(\mathbf{r}^0)$ of equation (7) with $s^{\min} = 5$ m. Contours are 50, 100, 200, 300 and 400 km. Combined geodetic resolution gives the size of 5 m slip features which can be resolved by the geodetic network given the specified precision of the survey. $L^{\min}(\mathbf{r}^0)$ scales like $1/\sqrt{s^{\min}}$, so patches with slip higher than 5 m can be resolved over smaller dimensions than the figure indicates. The lack of correlation between the patterns of VSP slip and $L^{\min}$ suggests that most of the peaks of slip are real, and not artifacts of the inversion. Any hidden moment for the 1960 rupture must occur outside of the 200 km contour to go undetected by the network. Because of the large tsunami generated by the event, substantial undetected offshore slip is likely.

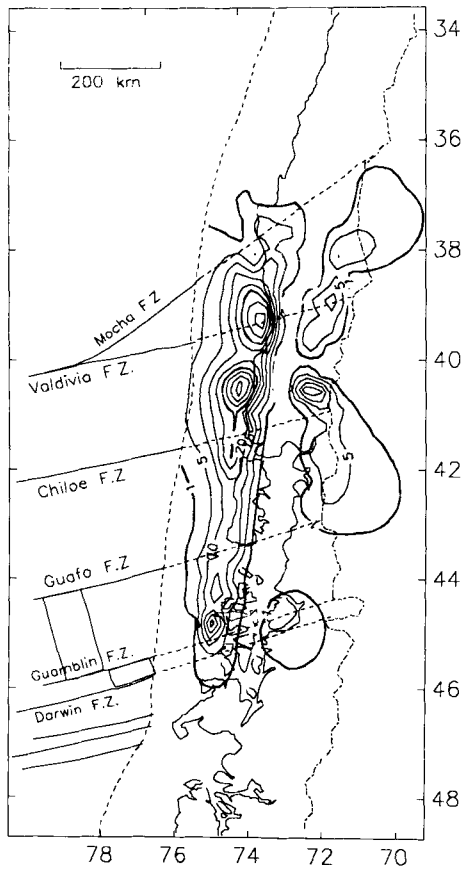

Figure 10. Map view of the VSP slip distribution and landward extension of Nazca Plate fracture zones. The 1960 rupture was sharply terminated at the intersection of major fracture zones to the north and south which likely define a segment boundary for this part of the Chile subduction zone. Fractures may also play a role in bounding asperties on the main interplate thrust zone.

patches are 100–300 km in size, have peak slips of 5–20 m and are required to match inland uplifts (compare Figs 5 and 7) and strain observations. Such down dip patches were also found by Linde & Silver (1989) in a 2-D variable slip analysis of Plafker's sea-level data. The resolving power of our network near the patches is good, so their dimensions and locations are probably reliable.

A number of questions concerning these patches arise: did the patches slip seismically over a few seconds or aseismically over months or years? Did slip occur coseismically within a few hours of the mainshock or was it a post-seismic phenomena generated sometime later within the 8 yr prior to Plafker's sea level measurements? Did the patches grow in place or did slip migrate down from the belt of major moment release?

Kanamori & Cipar (1974) associated event B, the long-period precursor to the mainshock, with deep moment release nearly equal to that of the mainshock (event C). It is tempting to identify our down dip patches with their long-period precursor; however, down dip moment release is only about one fourth of that of the main shallow region. Because the depth of the patches (80–110 km) is below the seismogenic zone in the area, we prefer the aseismic mechanism. Independent estimates of a 3 cm yr^{-1} uplift of the tide gauge at Puerto Montt during 1965 and 1970 (Wyss 1976) intimates that at least the southern patches are of slow post-seismic origin. Both post-seismic in-place growth and down dip migration of slip would have caused an uplift at the tide gauge at Puerto Montt of nearly 70 cm; however, down dip migration of the patch would have left behind a trail of moment release. The absence of slip just above these patches precludes down dip propagation from the main body. For in-place growth, dislocations transversing the half-width of a 100 km patch over an 8 yr period would have migrated with a speed of 6 km yr^{-1}. The nature of the northern down dip patch near the mainshock epicentre is not as clear because the tide gauge at Puerto Montt is too far away to constrain the time-scale of its formation. We suggest that the northern patch, being of similar size and depth as the southern patches, is also a slowly developing post-seismic feature.

Missing moment?

One implication of our geodetic model of the 1960 sequence concerns the total moment release. The VSP moment of 9.5×10^{22} N m is about one fifth of the value estimated for the foreshock–aftershock (events B, C and D) sequence from seismic methods [4.7×10^{23} N m according to Kanamori & Cipar (1974) and Kanamori (1977); 5.1×10^{23} N m according to Cifuentes & Silver (1989)]. Ward & Valensise (1989) demonstrated that, when unconstrained, VSP results replicate minimum model norm solutions. As such, the

method tends to put moment only at places where it can be best resolved. How much moment could there be missing from the VSP analyses? Satisfactory VSP models can be found with faults dipping anywhere between 15° and 25°. Geodetic moment increases from 6.4×10^{22} to 1.4×10^{23} N m with increasing dip in this range because each point-source is correspondingly deeper in the Earth. Seismicity (Kadinsky-Cade 1985) favours a shallow dip (≈10°–15°) for the upper 200 km of the fault where most of the moment release occurred, followed by a steepening to about 30°. If anything, curved faults following this seismicity distribution will have smaller geodetic moments than our 20° dipping planer model.

Errors in the uplift measurements are of the order of 20 per cent. From a geodetic perspective it would be difficult to increase moment release by much more than 20 per cent (2.0×10^{22} N m) anywhere the network has significant resolution without contradicting the data. Naturally, large amounts of moment can be hidden where the net has no resolution, say, outside of the 200 km contour in Fig. 9. Moment release outside this contour is nearly invisible. Because the spatial resolution of the network is fairly good, the only sites where moment could go undetected are north of 37°, south of 46°, down dip below 200 km depth, or at less than 20 km depth out to sea. Except for the last possibility, none of the locations is particularly attractive. In view of the damaging tsunami that accompanied the earthquake, substantial offshore slip was almost certainly overlooked. At the trench, 30 m of slip on a 20° dipping fault would produce 10.2 m of vertical uplift, about equal to the maximum tsunami height seen locally. If out to sea, the upper 50 km of the 900 km long fault uniformly slipped to this extent, the missing offshore moment would amount to 6.7×10^{22} N m. Considering errors in the data and sources of unmapped slip, it is not likely that the moment release for the entire 1960 sequence can be much larger than 1.8×10^{23} N m.

Satisfactory explanations for the discrepancy between geodetic and seismic moments are not immediately apparent; however, we believe that a smaller release for the 1960 sequence better fits the observed cycle of repeating large and occasional great events which characterize the boundary. Cifuentes & Silver's (1989) moment of 5.1×10^{23} N m placed on a fault 1000 km long and 400 km wide, would have expended 26 m of slip ($\mu = 5 \times 10^{10}$ Pa). If Nazca–South America plate convergence proceeds at the NUVEL-1 rate (8.4 cm yr^{-1}), such an event would consume the entire slip budget, both seismic and aseismic, over the 400 km wide boundary for over 300 yr. The geodetically determined moment (including 'missing slip') of 1.8×10^{23} N m, leaves 3.3×10^{23} N m in the budget, enough for a magnitude 9.1 event every century.

6 CONCLUSIONS

A total of 166 observations of sea level change, 130 measurements of elevation difference along a standard levelling line, and 16 determinations of strain from eight triangulation nets, provide an excellent view of the (quasi-)static source process of the great 1960 Chilean earthquake. These surface deformation data were employed in classical uniform slip fault models as well as more recently developed models that allow spatial variability of slip. Superpositions of elemental point-sources and a gradient technique with a positivity constraint form the foundation of variable slip analysis. The best USP model is 850 km long, 130 km wide, and dips 20°. Seventeen metres of fault displacement contributed to a USP moment of 9.4×10^{22} N m. The VSP model concentrates slip on a 900 km long, 150 km wide band parallel to the coast. Several peaks of slip and static stress drop with dimensions of 50–100 km appear in this band and are thought to represent major subduction zone asperities. Important fractures of the oceanic lithosphere bound the 1960 rupture and are offered as a potential source of fault segmentation within the Chilean subduction zone.

Apparently, great 1960-type events are not typical members of the ≈128 yr earthquake cycle in central Chile. The Nazca–South America boundary here is characterized by a variable rupture mode in which major asperities are completely broken by great earthquakes only once in four or five earthquake cycles. The more frequent large earthquakes that geographically overlap the great events, fill in between the locked zones.

Several patches of slip, isolated from the main body of moment release at depths of 80–110 km are found in the VSP model and are presumably indicative of aseismic slip. One patch at the northern end of the rupture (37°–40°S) is probably associated the initiation phase of the mainshock, although the time sequence of the relationship is unknown. Another down dip patch of slip between 40° and 43°S is responsible for the observed inland uplift and strains at those latitudes. Tide gauge records argue that this patch derived from in-place, post-seismic slip over a period of several years.

The geodetic moment of the VSP model totals 9.5×10^{22} N m, about one fifth of the value estimated using seismic methods. Because the VSP technique tends to produce minimum model norm results, moment could always be increased by forcing slip to locations not well resolved by the network. After accounting for changes in fault dip, errors in the data, and probable offshore slip, we feel that total moment for the 1960 sequence cannot be much larger than 1.8×10^{23} N m.

ACKNOWLEDGMENTS

We thank Ross Stein, Katharine Kadinsky-Cade, Ines Cifuentes, and Seth Stein for helpful comments. This work has been partially supported by National Science Foundation grants EAR 87-20328, INT 87-15242 and INT 88-22260, NASA CDP award NASA-560, W. M. Keck Foundation award 892 and Fondo Nacional de Ciencia y Tecnología 88-515. Contribution 75, C. F. Richter Laboratory/Institute of Tectonics, University of California, Santa Cruz, 95064.

REFERENCES

Barazangi, M. & Isacks, B. L., 1976. Spatial distribution of earthquakes and subduction of the Nazca plate beneath South America, *Geology*, **4**, 686–692.

Barrientos, S. E., 1988. Slip distribution of the 1985 central Chile earthquake, *Tectonophysics*, **145**, 225–241.

CERESIS, 1986. *Neotectonic Map of South America*, CERESIS–USGS, Lima, Peru.

Cifuentes, I., 1989. The 1960 Chilean earthquakes, *J. geophys. Res.*, **94**, 665–680.

Cifuentes, I. & Silver, P., 1989. Low-frequency source characteristics of the great 1960 Chilean earthquake, *J. geophys. Res.*, **94,** 643–664.

Davis, S. & Karzulovíc, J., 1963. Landslides at Lago Riñihue, *Bull. seism. Soc. Am.*, **53,** 1403–1414.

DeMets, C., Gordon, R. G., Argus, D. F. & Stein, S., 1990. Current plate motions, *Geophys. J. Int.*, **101,** 425–478.

Duda, S. J., 1963. Strain release in the circum-pacific belt, Chile: 1960, *J. geophys. Res.*, **68,** 5531–5544.

Duke, M. & Leeds, D., 1963. Response of soils, foundations, and earth structures to the Chilean earthquakes of 1960, *Bull. seism. Soc. Am.*, **53,** 309–357.

Herron, E. M., 1981. Chile margin near lat 38°: Evidence for a genetic relationship between continental and marine geologic features or a case of curious coincidences?, *Mem. geol. seism. Soc. Am.*, **154,** 755–760.

Housner, G. W., 1963. An engineering report on the Chilean earthquakes of May, 1960, *Bull. seism. Soc. Am.*, **53,** 219–223.

Kadinsky-Cade, K., 1985. Seismotectonics of the Chile Margin, *PhD thesis,* Cornell University, Ithaca, NY.

Kanamori, H., 1977. The energy release in great earthquakes, *J. geophys. Res.*, **82,** 2981–2987.

Kanamori, H., 1986. Rupture process of subduction-zone earthquakes, *Ann. Rev. Earth planet. Sci.*, **14,** 293–322.

Kanamori, H. & Cipar, J., 1974. Focal process of the great Chilean earthquake May 22, 1960, *Phys. Earth planet. Inter.*, **9,** 128–136.

Kanamori, H. & McNally, K. C., 1982. Variable rupture mode of the subduction zone along the Ecuador–Columbia Coast, *Bull. seism. Soc. Am.*, **72,** 1241–1253.

Linde, A. T. & Silver, P. G., 1989. Elevation changes and the great 1960 earthquake: support for aseismic slip, *Geophys. Res. Lett.*, **16,** 1305–1308.

Lomnitz, C., 1970. Major earthquakes and tsunamis in Chile during the period 1535 to 1955, *Geol. Rundsh.*, **59,** 938.

Lomnitz, C. & Hax, A., 1966. Clustering in aftershock sequences, in *The Earth Beneath the Continents,* Am. Geophys. Union Geophys. Mon. Ser. 10, pp. 502–508, eds Steinhart, J. S. & Smith, T. J., Washington, DC.

Minster, J. B. & Jordan, T. H., 1978. Present-day plate motions, *J. geophys. Res.*, **83,** 5331–5334.

Nishenko, S., 1985. Seismic potential for large and great interplate earthquakes along the Chilean and Southern Peruvian margins of south America: A quantitative reappraisal, *J. geophys. Res.*, **90,** 3589–3615.

Plafker, G., 1972. Alaskan earthquake of 1964 and Chilean earthquake of 1960: Implications for arc tectonics, *J. geophys. Res.*, **77,** 901–925.

Plafker, G. & Savage, J. C., 1970. Mechanism of the Chilean earthquakes of May 21 and 22, 1960, *Geol. Soc. Am. Bull.*, **81,** 1001–1030.

Press, F., Ben-Menahem, A. & Toksöz, N., 1961. Experimental determination of earthquake fault length and rupture velocity, *J. geophys. Res.*, **66,** 3471–4485.

Sievers, H. A., Villegas, G. & Barros, G., 1963. The seismic sea wave of 22 May 1960 along the Chilean coast, *Bull. seism. Soc. Am.*, **53,** 1125–1190.

Stein, S., Engeln, J. F., DeMets, C., Gordon, R. G., Woods, D. F., Lundgren, P., Argus, D., Stein, C. & Weins, D. A., 1986. The Nazca–South America convergence rate and the recurrence of the great 1960 Chilean earthquake, *Geophys. Res. Lett.*, **13,** 713–716.

Tichelaar, B. W. & Ruff, L., 1989. Variability in the depth of seismic coupling along the Chilean subduction zone, *EOS, Trans. Am. geophys. Un.*, **70,** 398.

Ward, S. N. & Barrientos, S. E., 1986. An inversion for slip distribution and fault shape from geodetic observations of the 1983, Borah Peak, Idaho, earthquake, *J. geophys. Res.*, **91,** 4909–4919.

Ward, S. N. & Valensise, G., 1989. Fault parameters and slip distribution of the 1915, Avezzano, Italy earthquake derived from geodetic observations, *Bull. seism. Soc. Am.*, **79,** 690–710.

Wieschet, W., 1963. Further observations of geological and geomorphic changes resulting from the catastrophic earthquake of May, 1960 in Chile, *Bull. seism. Soc. Am.*, **53,** 1237–1257.

Wright, C. & Mella, A., 1963. Modifications to the soil pattern of south-central Chile resulting from seismic and associated phenomena during the period May to August 1960, *Bull. seism. Soc. Am.*, **53,** 1367–1402.

Wyss, M., 1976. Local changes of sea level before large earthquakes in South America, *Bull. seism. Soc. Am.*, **66,** 903–914.

APPENDIX

Horizontal displacements at position $\mathbf{r} = (x, y, 0)$ due to a point moment tensor at $\mathbf{r}^0 = (0, 0, h)$ in an elastic half-space. We assume the following conventions: coordinates x, y, z are north, east and down; azimuth $\theta = \tan^{-1}(y/x)$ is measured north to east; $R = \sqrt{x^2 + y^2 + h^2} = \sqrt{r^2 + h^2}$; $\hat{r} = (\hat{x}x + \hat{y}y)/r$; and $\hat{\theta} = \hat{z} \times \hat{r}$.

$$\begin{aligned}\mathbf{u}(\mathbf{r}, \mathbf{r}^0) = {} & \hat{r}\frac{(M_{xx} + M_{yy})}{8\pi\mu} I_0^a(r, h) - \hat{r}\frac{M_{zz}}{4\pi\mu} I_0^b(r, h) \\ & - \hat{r}\frac{M_{xz}\cos\theta + M_{yz}\sin\theta}{4\pi\mu} I_1(r, h) \\ & + \hat{r}\frac{(M_{xx} - M_{yy})\cos 2\theta + 2M_{xy}\sin 2\theta}{8\pi\mu} I_2^a(r, h) \\ & + \hat{\theta}\frac{(M_{yy} - M_{xx})\sin 2\theta + 2M_{xy}\cos 2\theta}{4\pi(\lambda + \mu)} I_2^b(r, h)\end{aligned}$$

where

$$I_0^a(r, h) = \frac{r}{R^3}\left[\frac{\lambda + 2\mu}{\lambda + \mu} - \frac{3h^2}{R^2}\right]$$

$$I_0^b(r, h) = \frac{r}{R^3}\left[\frac{\lambda}{\lambda + \mu} - \frac{3h^2}{R^2}\right]$$

$$I_1(r, h) = \frac{6hr^2}{R^5}$$

$$\begin{aligned}I_2^a(r, h) = {} & \frac{r}{R^3}\left[\left(\frac{\lambda + 2\mu}{\lambda + \mu} - \frac{3h^2}{R^2}\right)\right. \\ & \left. + \frac{2}{(R + h)^2}\left(\frac{\lambda R^2}{\lambda + \mu} + h(2R + h)\right)\right]\end{aligned}$$

$$I_2^b(r, h) = \frac{(R - h)^2}{r^3 R}$$